polymers

MDPI

Article

Poly(carbazole-co-1,4-dimethoxybenzene): Synthesis, Electrochemiluminescence Performance, and Application in Detection of Fe^{3+}

Pengchong Hou [1], Xian Zhang [1,*], Qian Lu [1,*], Shunwei Chen [1], Qiang Liu [1], Congde Qiao [1] and Hui Zhao [2,*]

[1] School of Materials Science and Engineering, Qilu University of Technology, Shandong Academy of Sciences, Jinan 250353, China; hou17806022585@163.com (P.H.); swchen@qlu.edu.cn (S.C.); yeah21138@126.com (Q.L.); cdqiao@qlu.edu.cn (C.Q.)

[2] School of Chemical Engineering, Sichuan University, Chengdu 610065, China

* Correspondence: zhangx@qlu.edu.cn (X.Z.); qluqlu@qlu.edu.cn (Q.L.); zhaohuichem@scu.edu.cn (H.Z.); Tel.: +86-134-7596-2648 (X.Z.); +86-187-6613-0996 (Q.L.)

Abstract: In this study, four polycarbazole derivatives (PCMB-Ds) with different alkyl side chains were designed and synthesized via Wittig–Horner reaction. A novel solid-phase electrochemiluminescence (ECL) system was prepared by immobilizing PCMB-D on an indium tin oxide (ITO) electrode with polyvinylidene fluoride (PVDF) in the presence of tripropylamine (TPrA). It could be found that the increase in alkyl side chain length had little effect on the ECL signal of PCMB-D, while the increase in the degree of polymerization (DP) greatly enhanced the ECL signal. Furthermore, the P-3/ITO ECL sensor based on the polyoctylcarbazole derivative (P-3) with the best ECL performance was successfully constructed and detected Fe^{3+} under the optimal experimental conditions. The ECL signal steadily diminished with the increased concentration of Fe^{3+} because of the competition and complexation between Fe^{3+} and P-3 under the condition of pH 7.4. This P-3/ITO platform could realize a highly sensitive and selective detection of Fe^{3+} with a wide detection range (from 6×10^{-8} mol/L to 1×10^{-5} mol/L) and low detection limit of 2×10^{-8} mol/L, which could allow the detection of Fe^{3+} in multiple scenarios, and would have a great application prospect.

Keywords: electrochemiluminescence; polycarbazole; ECL sensor; detection; Fe^{3+}

Citation: Hou, P.; Zhang, X.; Lu, Q.; Chen, S.; Liu, Q.; Qiao, C.; Zhao, H. Poly(carbazole-co-1,4-dimethoxybenzene): Synthesis, Electrochemiluminescence Performance, and Application in Detection of Fe^{3+}. *Polymers* **2022**, *14*, 3045. https://doi.org/10.3390/polym14153045

Academic Editor: Isao Yamaguchi

Received: 2 June 2022
Accepted: 22 July 2022
Published: 27 July 2022

1. Introduction

Fe^{3+} is essential for the balance of various environmental and biological systems [1]. In the human body, Fe^{3+} has unique significance in oxygen transport and metabolism [2], cellular enzymatic reactions [3], DNA repair, etc. [4]. The content of Fe^{3+} should be less than 0.3 mg/L in the environment, 5.36 μmol/L in drinking water, and 70~150 μg/L in serum [5]. Deficiency or excessive use of Fe^{3+} can disrupt normal biological processes, leading to anemia, decreased immunity, infection, Parkinson's, Alzheimer's, cancer, etc. Consequently, the rapid detection and real-time monitoring of the concentration of Fe^{3+} are of great significance to protect the ecological environment and people's lives and health. Therefore, the development of suitable detecting methods and sensors for the detection and monitoring of the concentration of Fe^{3+} has received extensive attention.

At present, the main methods for detecting Fe^{3+} are atomic absorption spectroscopy [6], gas chromatography, and ultraviolet–visible spectrophotometry [7], but their detection process is complicated [8] and the equipment is expensive and requires relatively skilled professionals [9], while the ECL analysis in the electrochemical sensor method has developed rapidly because of its convenient and fast operation, high sensitivity [10] and low cost [11], and this method has attracted more and more attention [12]. Therefore, it is very necessary and promising to design new ECL reagents to detect Fe^{3+}.

Although the ECL method has already been used, it has only been used in the analysis and testing field in recent years [13]. ECL analysis [14] is the latest product of the

combination of chemiluminescence, electrochemistry, bioanalysis, microelectronic technology [15], and sensing technology, showing the unique advantages of high sensitivity, simple operation, strong controllability, quick and easy analysis [16] and great potential in the field of clinical [17], agricultural [18], and environmental monitoring [19]. In terms of ECL active materials, $Ru(bpy)_3^{2+}$ [20], Luminol [21], iridium complexes [22], quantum dots [17], and other inorganic materials [23] have relatively stable luminescence and mature research, but their luminescence brightness and lifetime need to be improved, and their excitation potential is high [9]. Recently [24], CPs have attracted the attention of many researchers. CPs had always been regarded as insulating materials until Burroughes of Cambridge University first observed the ECL signal of poly (phenylene vinylene) (PPV) in 1990 [25], which opened a new era in the research of CPs as ECL materials. Since then, more and more polymer ECL active materials such as polypyrrole (PPY) [26], polyvinyl carbazole (PVK) [27], polythiophene (PT) [28] and polyfluorene (PF) were gradually observed and exhibited unique optical and electrical properties, such as good expandability, strong light trapping ability, low energy consumption, high fluorescence quantum yield, great biocompatibility, low price, and other unmatched advantages [29]. However, most of the traditional CPs used for ECL bioassays were liquid phase and might bind non-specifically with other substances in the aqueous phase, which would affect the detection accuracy. Compared with the liquid phase, the luminescent reagent of the solid-phase system was separated from the object to be detected, improving detection accuracy [30] and saving the consumption of CPs. Therefore, it is very meaningful to design a solid-phase ECL sensing platform based on a novel CP ECL material to realize the detection of Fe^{3+}.

Polycarbazole [31] is a linear conjugated polymer with an aromatic heterocyclic ring containing nitrogen atoms. Its conjugated structure is extended by a benzene ring, which is similar to a molecular wire, giving electrical conductivity [32]. The carbazole ring located in the main part of the polymer is conducive to carrier migration. In addition, the three-dimensional structure of polycarbazole provides excellent solubility and film-forming properties, high concentration of active groups, good signal amplification performance, and chemical stability [33]. More importantly, their molecular structure and surface functional groups are easily designed and tailored. For example, carbazole can easily be introduced to a variety of groups on the nitrogen atom, and modified at the position of third and sixth, so it is a very promising ECL material. In addition, the excited state generated by the electrification of polycarbazole may interact with strong oxidation of Fe^{3+}, which is likely to affect the ECL signal of the system, thereby this system may be applied to detect Fe^{3+}.

In addition, the ECL signals are closely related to the structure of CPs. The proper CP structure will help to improve the sensitivity of ECL biosensors. Herein, poly(ethylcarbazole-co-1,4-dimethoxybenzene) (P-1), poly(butylcarbazole-co-1,4-dimethoxybenzene) (P-2), poly(octylcarbazole-co-1,4-dimethoxybenzene) (P-3) and poly(hexadecylcarbazole-co-1,4-dimethoxybenzene) (P-4) were successfully synthesized based on Wittig–Horner reaction. This paper also discusses the relationship between the ECL signal and the structure of PCMB-D with different alkyl side chains and different DPs. In addition, PVDF acted as a binder between PCMB-D and ITO to obtain a more stable ECL signal. Furthermore, a solid-phase ECL system of PCMB-D on the electrode for detecting Fe^{3+} was constructed, and the detection mechanism was investigated. In our case, PCMB-D is expected to be a type of novel ECL reagent to impel the development of the CP ECL analysis method.

2. Materials and Methods

2.1. Materials

The ITO used in this experiment was purchased from Liaoning Huite Optoelectronics Technology Co, Ltd., Anshan City, China with a thickness of 0.7 mm, a transmittance of 85%, a resistance of 6–7 ohms, and a temperature resistance of 320 °C. Ethyl acetate (EtOAc), tetrahydrofuran (THF), dimethylketone (DMK), methyl alcohol (MT), *N*, *N*-dimethylformamide (DMF), acetonitrile (AN), *N*-methylpyrrolidone (NMP), PVDF and other chemicals were bought from commercial suppliers. All solvents used in this paper

were all analytical purity reagents. Ultrapure water was used throughout the experiments. It is worth mentioning that the electrode used in this experiment is ITO conductive glass. The ECL signal in this experiment is positively correlated with the aggregation state and coverage area of the polymer, and the larger modifiable area of ITO is convenient for the collection of ECL signals. In addition, the transparent electrode facilitates observations of the film formation status on the site.

2.2. Synthesis of PCMB-D

The synthetic procedure of a series of PCMB-Ds containing the same conjugated backbone with different alkyl side chains is shown in Scheme 1a. 9H-carbazole-3,6-dicarbaldehyde (M1), 3,6-diformyl-9-butylcarbazole (M2), 3,6-diformyl-9-octylcarbazole (M3), and 3,6-diformyl-9-hexadecylcarbazole (M4) are synthesized according to the previous literature [34]. P-1, P-2, P-3, and P-4 are synthesized via Wittig–Horner by combining 2,5-di-(ethoxy phosphoryl methylene)-1,4-dimethoxybenzene (M5) and M1, M2, M3, and M4, respectively. The relevant ^{1}H NMR spectra, ^{13}C NMR spectra, and FTIR are observed in Figures S1–S17. Gel permeation chromatographic (GPC) data are shown in Table 1.

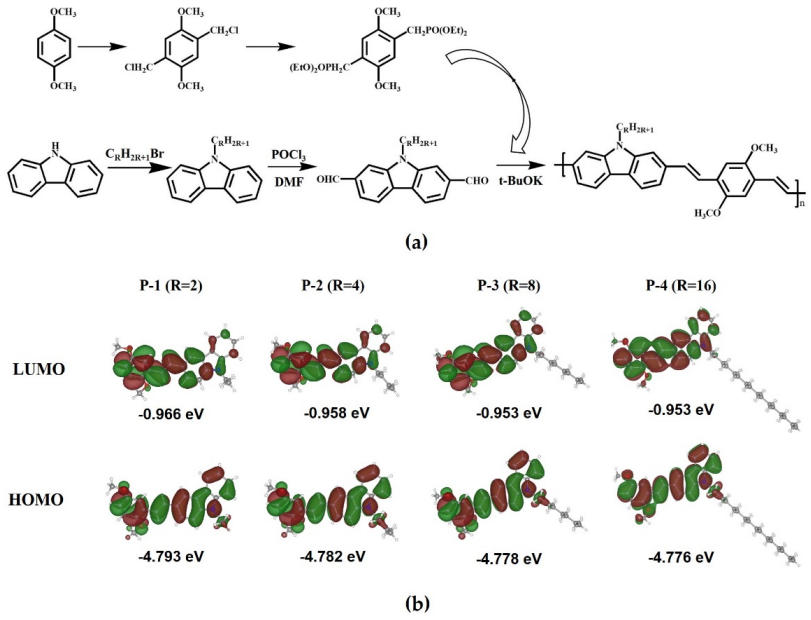

Scheme 1. (**a**) Synthetic route of the PCMB-D; (**b**) calculation of spatial distributions of the highest occupied molecular orbital (HOMO) and the lowest unoccupied molecular orbital (LUMO) in structural units of P-1, P-2, P-3, and P-4.

Table 1. GPC data of PCMB-D used.

PCMB-D	Mn (g/mol)	Mw (g/mol)	Mz (g/mol)	PDI	DP
P-1	2.347×10^4	2.548×10^4	4.323×10^4	1.086	57
P-2	3.023×10^4	3.383×10^4	7.461×10^4	1.119	69
P-3	3.725×10^4	4.034×10^4	6.226×10^4	1.083	75
P-4	1.936×10^4	2.106×10^4	2.809×10^4	1.088	32
P-3′	2.325×10^4	2.514×10^4	3.206×10^4	1.082	47
P-3″	1.339×10^4	1.607×10^4	2.209×10^4	1.200	27

2.3. Measurement

^{1}H NMR (400 MHz) spectra and ^{13}C NMR (101 MHz) spectra were recorded on a Bruker Avance 400 spectrometer in deuterated chloroform ($CDCl_3$) and dimethyl sulfoxide (DMSO) with tetramethylsilane (TMS) internal standard as reference. FTIR data for the PCMB-D were obtained using a Nicolet iS10 spectrometer (Thermo Fisher Scientific Inc.,

Waltham, MA, USA) equipped with an attenuated total reflection (ATR) accessory. The FTIR spectra were recorded in the range of 400 to 4000 cm^{-1} with a resolution of 4 cm^{-1} and 16 scans. The data were analyzed with Omnic software. The molecular weights and polymer dispersity indexes (PDI = Mw/Mn) were measured with PL-120 model permeation gel chromatography in DMF at room temperature using a calibration curve of polystyrene standard. The melting point (Mp) of the monomers was obtained by the RD-1 melting point tester. Thermal gravimetric analysis (TGA, Mettler Toledo, Switzerland) was used to test the thermal stability of the PCMB-D. TGA was carried out in N_2 atmosphere from 100 °C to 800 °C with a heating rate of 10 °C/min. Ultraviolet–visible (UV–Vis) absorption and fluorescence (FL) spectra were collected on a Shimadzu UV-2500 spectrophotometer and Hitachi F-7000 Fluorescence Photometer, respectively. Cyclic voltammetry (CV) curves and ECL signals were recorded on the MPI-E analysis system of Xi'an Remax Analytical Instrument Co, Ltd., Xi'an, China, equipped with a platinum wire and an Ag/Agcl as the auxiliary electrode and reference electrode, respectively.

2.4. Fabrication of ECL Sensor

Prior to fabrication of the ECL system, the ITO glass electrodes with a length of 2 cm and width of 1 cm were immersed in acetone, ethanol, and ultrapure water, and ultrasonically cleaned for 15 min. Then, the cleaned ITO was dried under a stream of N_2 for usage. PCMB-D and PVDF were dissolved in NMP together. The mixture was sonicated for 30 min, and then ball milled at 434 rpm for 4 h at room temperature. The ball-milled sample was coated immediately and uniformly on the dry ITO, and then baked at 90 °C for 12 h in a vacuum state. The modified ITO as a working electrode was immersed into 0.02 mol/L TPrA (0.1 mol/L PBS, pH = 7.4) for Fe^{3+} detection. The high voltage and scan rates were 800 V and 1 V/s, respectively.

3. Results and Discussion

3.1. Synthesis and Characterization

PCMB-D were synthesized via Wittig–Horner [34] as described in Scheme 1a. The structures of the polymers were characterized by ^{1}H NMR, ^{13}C NMR, and FTIR (Figures S1–S17). In the case of P-3, as depicted in Figures S3 and S10, the chemical shift at δ = 10.12 ppm was assigned to the aldehyde group of M3, and it completely disappeared in the ^{1}H NMR spectrum of P-3. In addition, the chemical shift at δ = 6.78 ppm in ^{1}H NMR of Figure S10, the absorption spectrum at 123 ppm in the ^{13}C NMR of Figure S11, and the stretching vibration and flexural vibration of C=C at 1600 cm^{-1} and 798 cm^{-1} in FTIR are characteristic of C=C forming. In addition, the stretching vibration of C-O at 1208 cm^{-1}, alkyl stretching vibrations of C-H at 2929 cm^{-1}, and the stretching vibrations of C-H of aromatic rings (1601 cm^{-1}) further proved that P-3 was successfully prepared by Wittig–Horner reaction based on M3 and M5. The similar deductions of other polymers could be obtained by comparing the ^{1}H NMR, ^{13}C NMR, and FTIR spectra of other monomers with their target polymers.

Based on the large delocalization of polycarbazole, a charge transfer bridge of C=C bond and a strong electron-donating group -OCH_3 were introduced, which provide delocalized transfer conditions for electrons and make the PCMB-D exhibit unique optical and electrical properties. UV–visible and emission spectra of P-1, P-2, P-3, and P-4 in different polar solvents are presented in Table 2 and Figure S18. As shown in Figure S18, P-1, P-2, P-3, and P-4 all have a broad absorption peak, and their maximum absorption wavelengths in NMP are 420, 420, 418, and 415 nm, respectively, which may correlate with the π–π* transition of the PCMB-D backbone. Based on an excitation wavelength of 418 nm, the maximum wavelengths of emission of P-1, P-2, P-3, and P-4 are 486, 486, 485, and 485 nm, respectively. The energy between the excitation and emission state of PCMB-D is slightly different, which is closely associated with the conjugated structure of PCMB-D. PCMB-Ds have good solubility in common organic solvents and large Stokes shifts. The Stokes shifts in different solvents are from 63 nm to 114 nm in Table 2. As we all know, a large

Stokes shift (typically over 80 nm) is beneficial to reduce error and maintain the accuracy of detection [34]. The absorption wavelengths of P-1, P-2, P-3, and P-4 are firstly blue-shifting and then red-shifting with increasing solvent polarity, indicating that the charge transfers for four PCMB-Ds are almost the same. Particularly, PCMB-Ds in NMP exhibit excellent absorption and fluorescence properties (Figure S18). For example, the maximum absorption wavelengths of P-3 in EtOAc, THF, DMK, MT, DMF, and AN are 390.4, 412, 362, 363, 408, 362, and 418 nm, and the corresponding maximum absorbances are 0.181, 0.281, 0.149, 0.174, 0.225, 0.125, and 0.28, respectively, which may be due to NMP's five-membered ring and strong polarity, which makes the π electrons more easily excited, and improves energy conduction between molecules. In addition, although polymer has limited solubility, PCMB-D in this experiment can be completely dissolved in NMP (Figure S19). Meanwhile, considering the good solubility of NMP for PVDF, NMP is selected as a good solvent for PCMB-D in this experiment, and P-3 appears as a bright yellow-green color in NMP as shown in Figure S19. At the same time, P-3 has an obvious fluorescence phenomenon whether it is powder or liquid, but Figure S20 shows that the fluorescence intensity of P-3 in NMP decreases with the addition of water, which illustrates that P-3 has an aggregation-induced quenching effect. Additionally, the Mp values of M1-M5 are 113 °C, 104 °C, 94 °C, 91 °C, and 115 °C, respectively. As shown in Figure S21, PCMB-D only has a weight loss rate of 10% at about 400 °C and, in particular, P-3 can still maintain good condition at 41 °C, and retains 90% at 448 °C. Thereafter, the polymer backbone may degrade due to the high reactivity of C=C, and there is still a 50% carbon residue rate around 600 °C. In addition, P1, P-2, and P-4 also exhibit good thermal stability like P-3, which is closely related to their DP and narrow PDI, indicating that PCMB-Ds have the potential to be used as ECL materials. Overall, PCMB-Ds will be an appropriate electrode modification material in the field of ECL owing to their good luminous performance and stability.

Table 2. Photoluminescence performance of PCMB-D in different solvents.

PCMB-D	Solvents	λ_{abs} [1] (nm)	A_{abs} [2]	λ_{em} [3] (nm)	I_{em} [4]	Stokes Shift (nm)
P-1	EtOAc	407.4	0.383	474	2137	66.6
	THF	415.8	0.521	484	3659	68.2
	DMK	383	0.371	476	2249	93
	MT	388	0.396	475	495.5	87
	DMF	408	0.45	484	2621	76
	AN	366	0.324	478	983.3	112
	NMP	420	0.557	486	5430	66
P-2	EtOAc	406.8	0.163	475	1882	68.2
	THF	416	0.202	479	3066	63
	DMK	402	0.133	477	1590	75
	MT	378	0.132	474	229.5	96
	DMF	410	0.171	483	1488	73
	AN	366	0.129	478	773.6	112
	NMP	420	0.21	486	3202	66
P-3	EtOAc	390.4	0.181	473	1325	82.6
	THF	412	0.281	478	3578	66
	DMK	362	0.149	474	829.4	112
	MT	363	0.174	438	163.4	75
	DMF	408	0.225	483	1201	75
	AN	362	0.125	474	302.9	112
	NMP	418	0.28	485	2839	67
P-4	EtOAc	359	0.151	473	2396	114
	THF	408	0.255	477	5145	69
	DMK	374	0.136	475	1793	101
	MT	363	0.174	467	182.7	104
	DMF	407	0.247	482	1468	75
	AN	362	0.156	475	357.3	113
	NMP	415	0.278	485	3110	70

[1] The maximum absorption wavelength of PCMB-D in different solvents. [2] The maximum absorbance of PCMB-D in different solvents. [3] The maximum wavelength of emission of PCMB-D in different solvents. [4] The maximum fluorescence intensity of PCMB-D in different solvents.

3.2. Construction and Characterization of PCMB-D/ITO

After cleaning the ITO, PCMB-D/ITO was constructed by modifying PCMB-D and PVDF on ITO, and the ECL platform was formed with PCMB-D/ITO as the working electrode, platinum wire electrode as the auxiliary electrode, and Ag/Agcl as the reference electrode. The ECL performance of PCMB-D was similar, and P-3 was chosen as an example because of its best thermal stability, excellent photoluminescence, and ECL performance. As illustrated in Figure 1, the ECL signals could not be found without PCMB-D and TPrA, and showed a better signal when P-3-modified ITO was immersed in TPrA. This shows that P-3 and TPrA as co-reactants are indispensable for the ECL platform.

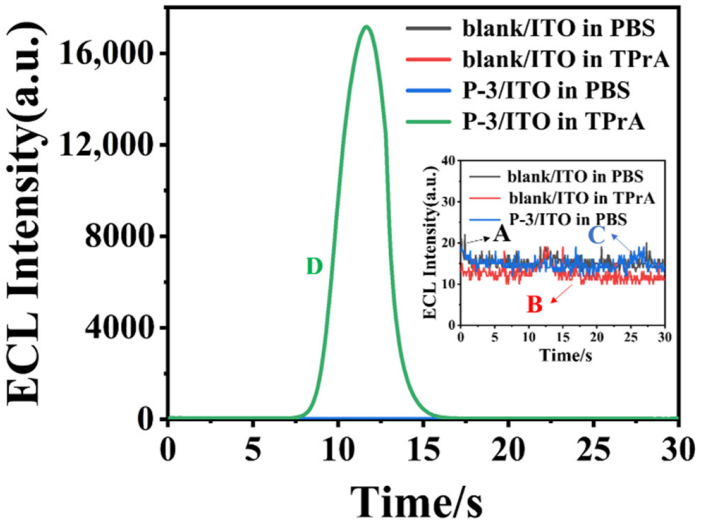

Figure 1. ECL signals of the constructed platform sensor: (A) ECL signals of blank/ITO in PBS; (B) ECL signals of blank/ITO in TPrA; (C) ECL signals of P-3/ITO in PBS; (D) ECL signals of P-3/ITO in TPrA. The inset is the enlarged ECL signals of blank/ITO in PBS, blank/ITO in TPrA, and P-3/ITO in PBS.

3.3. ECL Performance of P-3/ITO

The excellent thermal stability and optical properties of PCMB-D indicate that this type of material has the potential to be used as an ECL reagent. Unfortunately, when scanning cycles continued, the ECL strength of the PCMB-D decreased. The possible reason is the lack of strong force connection between the PCMB-D and ITO, causing the coating to peel off and making accurate detection difficult. In order to solve this problem, PVDF binder was introduced. PVDF and CPs were dissolved in NMP and modified on ITO. Using P-3 as an example, it was found that the cycle stability of the P-3/ITO can be significantly improved when the ratio of P-3 to PVDF is 7:3, shown in Figure 2a.

In order to further improve the ECL performance of P-3/ITO and obtain better ECL signals, the multi-parameter optimization of this ECL platform has been extensively studied. The effects of co-reactant, pH, number of modifier layers, and drying temperature on the solid-phase ECL sensor were mainly investigated. Figure 2b shows that P-3/ITO has no ECL signal in PBS and common co-reactants $K_2S_2O_8$ and oxalic acid, but exhibits a clear ECL signal in the presence of TPrA. The optimal concentration of TPrA was also explored. P-3/ITO produced a superior ECL signal in 0.02 mol/L TPrA, as seen in Figure 2c.

In the measuring system, the pH environment of the buffer solution has a significant impact on the electron transfer rate of the electrode surface. As shown in Figure 2d, the ECL signal increases and then declines as the pH increases, and the highest value appears at about pH = 7. It was further found that pH = 7.4 was optimal for the formation of high-energy neutral amine radical reducing species.

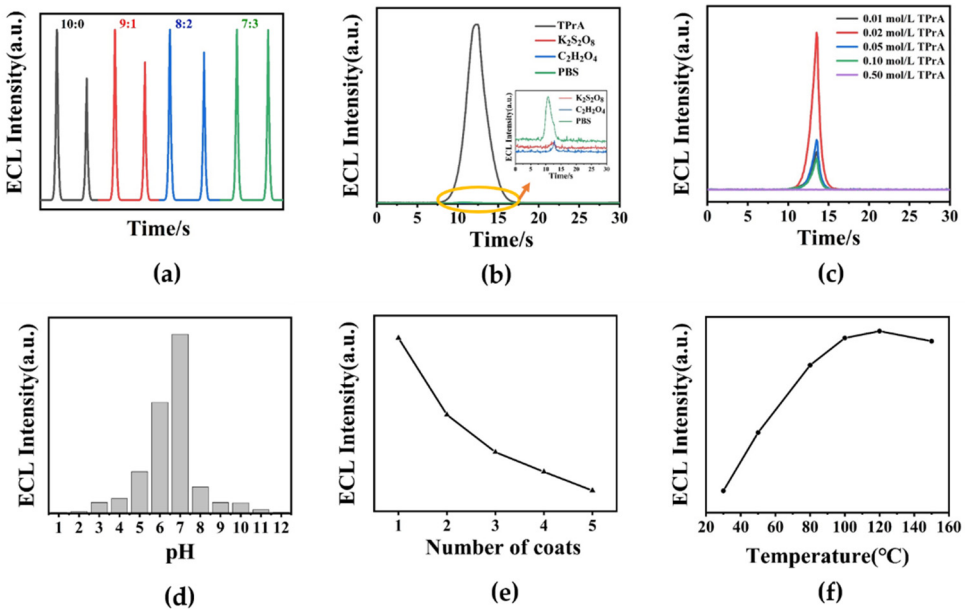

Figure 2. ECL intensity of P-3/ITO under different conditions: (**a**) different ratios of P-3:PVDF in electrode modifiers (10:0; 9:1; 8:2; 7:3); (**b**) different co-reactants (TPrA, $K_2S_2O_8$, $C_2H_2O_4$, PBS); (**c**) different concentrations of TPrA (0.01 mol/L, 0.02 mol/L, 0.05 mol/L, 0.10 mol/L, 0.50 mol/L); (**d**) different pH environments (pH = 1~12); (**e**) the number of layers (1~5) modified by P-3 on the ITO electrode; (**f**) different drying temperatures (30 °C, 50 °C, 80 °C, 100 °C, 120 °C, 150 °C).

In general, the ECL signal will be amplified with a higher concentration and bigger loading of P-3 on ITO. Nevertheless, as demonstrated in Figure 2e, more layers of P-3 modified on the ITO surface increase the resistance and decrease the ECL signal. A better signal is obtained by modifying a thin layer of P-3 on ITO with a thickness of 27 μm. In addition, as shown in Figure 2f, the ECL signal of P-3/ITO increased firstly and then decreased slightly with the increased drying temperature. As a result, the proper drying temperature was 120 °C.

The ECL performance of P-3 is evaluated under the above conditions. As shown in Figure 3a, P-3/ITO can emit an obvious ECL signal in 0.02 mol/L TPrA (0.1 mol/L PBS, pH = 7.4). Corresponding to ECL at an oxidation state of 1.0 V (Figure 3b), the excitation potential of P-3/ITO is 0.86 V (Figure 3c). The excitation potential of this type of polymer is relatively small, which shows that the P-3/ITO can be excited by a lower voltage. This can effectively save resources and reduce the damage to other components during the detection.

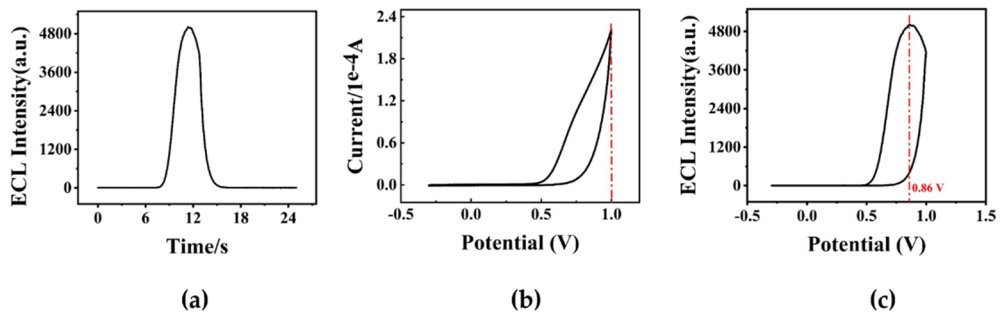

Figure 3. (**a**) ECL–time curves; (**b**) CV curves; (**c**) ECL–potential curves of P-3/ITO in 0.02 mol/L TPrA (0.1 mol/L PBS, pH = 7.4).

3.4. The Relationship between ECL Properties and the Structure of PCMB-D

To evaluate the effect of different alkyl side chains and other structural factors on the ECL properties, the ECL system of PCMB-D/ITO solid phase is constructed. As shown in 5b, the ECL response has good potential cycling stability for P-1, P-2, P-3, and P-4. In addition, Figure 4a,b show that the ECL signal intensity of P-3 is the best, which may be attributed to the alkyl side chains or DP.

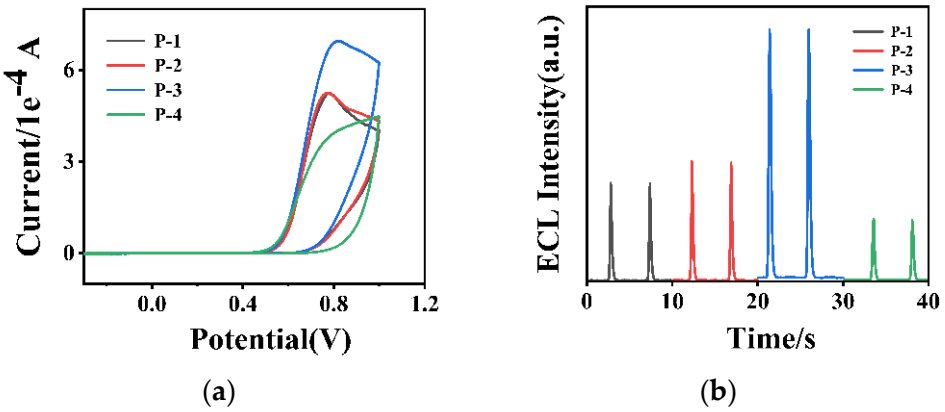

Figure 4. (**a**) CV curves; (**b**) ECL curves of PCMB-D/ITO in 0.02 mol/L TPrA (0.1 mol/L PBS, pH = 7.4).

To better understand the electronic properties and explore the influence of alkyl side chain length on ECL signal, density functional theory (DFT) calculations were performed [35]. Ground-state geometry optimization was carried out for P-1, P-2, P-3, and P-4 structures, which contain varying numbers of structural units (see structures in Scheme 1b) at the ωB97XD/6-311G(d,p) level [36,37]. As shown, the HOMO and LUMO of each structure basically overlap in space with each other, implying that there is no obvious intramolecular charge transfer phenomenon in these molecules [17], and thus proving that the PCMB-D/ITO is a co-reactive ECL system. In addition, the HOMO–LUMO gaps of the structural models of P-1, P-2, P-3, and P-4 show a very small variation, 3.827, 3.824, 3.824, and 3.823 eV, respectively (Figure S22). Therefore, the length of the side alkyl chain of PCMB-Ds shall impart limited influence on their ECL performance. Furthermore, in Figure 4 and Table 1, the signal of P-3 is the best, and that of P-4 is the weakest. The DP of P-3 (3.725×10^4) is higher than that of P-4 (1.936×10^4), which implies that higher DP of PCMB-D will help to improve the ECL performance. To further verify this conjecture, we compared the FL properties and ECL properties of three polyoctylcarbazole derivatives (P-3, P-3′, and P-3″) with different DPs. As shown in Figure 5, the emission peaks of P-3, P-3′, and P-3″ were 484 nm, 485 nm, and 487 nm at an excitation wavelength of 418 nm, respectively. A slight red shift was found, and this could be attributed to reduced DP. Moreover, the FL intensity and ECL signal of P-3 were the best, which indicated that the larger DP was beneficial to obtaining a better ECL signal, and the alkyl side chain had a small influence. In addition, the FL and ECL intensity of P-3″ was the weakest, but it was still fluorescent material. This further verified that a higher DP can obtain a better FL and ECL signal. This supplies an idea for the future directional synthesis of CP ECL materials with better performance.

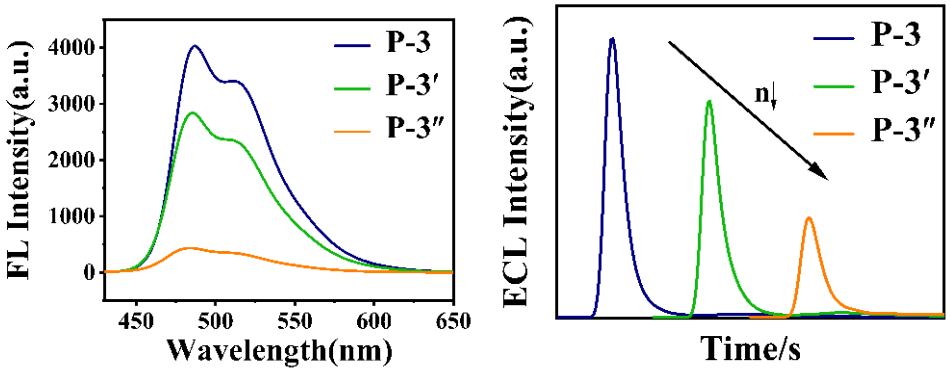

Figure 5. (**a**) Fluorescence emission spectra excited at 418 nm; (**b**) ECL curves of P-3, P-3′, and P-3″.

3.5. ECL Detection of Fe^{3+} with the P-3/ITO Sensor

From the above analysis results, P-3 has better thermal stability and ECL properties than other PCMB-D; in addition, the 9th position of P-3 is easily attacked, and the excited state of P-3 may undergo a redox reaction with strong oxidation of Fe^{3+}, so a P-3/ITO solid-phase ECL sensing platform was constructed for subsequent sensing tests of Fe^{3+}. In Figure 6a, the ECL intensity of P-3/ITO gradually declines after adding Fe^{3+} to the reaction solution, and the red-brown precipitation was found at the same time. The ECL signal of P-3/ITO was linearly fitted to the logarithm of concentration of Fe^{3+} (from 6×10^{-8} mol/L to 1×10^{-5} mol/L), and the linear equation was obtained from Figure 6b:

$$I = -2081 - 618 \log c\,(Fe^{3+})\ (R^2 = 0.954) \quad (1)$$

where $\log c\,(Fe^{3+})$ is the logarithm of concentration of Fe^{3+}, and I is the ECL intensity of P-3/ITO to the concentration of Fe^{3+}.

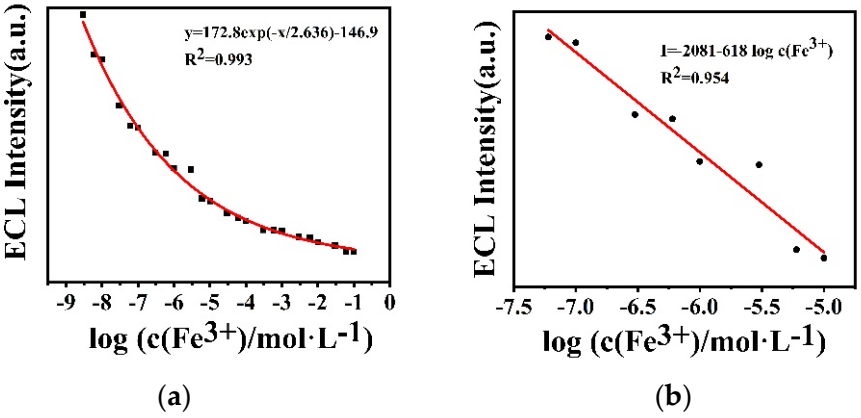

Figure 6. (**a**) ECL curves of PCMB/ITO in 0.02 mol/L TPrA (0.1 mol/L PBS, pH = 7.4) containing different concentrations of Fe^{3+}; (**b**) the linear fitting curve of ECL intensity of P-3/ITO to the concentration of Fe^{3+} from 6×10^{-8} mol/L to 1×10^{-5} mol/L.

Furthermore, this limit of detection (LOD) was calculated according to the following formula:

$$LOD = 3\,\sigma\ /\ k \quad (2)$$

where σ is the deviation of response values, and k is the slope of the standard curve.

The calculated LOD is 2×10^{-8} mol/L, allowing for quantitative detection of Fe^{3+} from 6×10^{-8} mol/L to 1×10^{-5} mol/L. These data showed that the P-3/ITO platform

is able to meet the detection requirements of Fe^{3+} in drinking water (5.36 μmol/L), in the environment (0.3 mg/L), and in serum (70~150 μg/L).

Compared with many methods reported for Fe^{3+} detection in many studies, our method has a wider detection range and lower limit, as shown in Table 3.

Table 3. Comparison of Fe^{3+} detection methods.

Reaction Interface	Linear Range (μmol/L)	LOD (μmol/L)	Ref.
carbon dots	8~80	3.8	[38]
N-CQD	0~500	0.15	[39]
DSW-CD	0~20	0.128	[40]
DPA-GQD	4~1800	1200	[41]
N-doped CD	10~300	0.9	[42]
PCMB-D	0.06~10	0.02	this work

N-CQD: nitrogen-doped carbon quantum dot; DSW-CD: durian shell waste carbon dot; DPA-GQD: D-penicillamine graphene quantum dot; N-doped CD: N-doped carbon dot.

3.6. Stability and Selectivity of P-3/ITO Sensors

In order to explore the stability of P-3/ITO, this experiment recorded the ECL curve of P-3/ITO in 0.02 mol/L TPrA (0.1 mol/L PBS, pH = 7.4) under long-time scanning. The result is shown in Figure 7a that the ECL signal gradually increased until 140 s when the P-3/ITO was energized. Then, the ECL intensity reached the maximum value and maintained stability after 25 cycles of continuous scanning for 9 min. This indicates that the P-3/ITO ECL sensor has good stability.

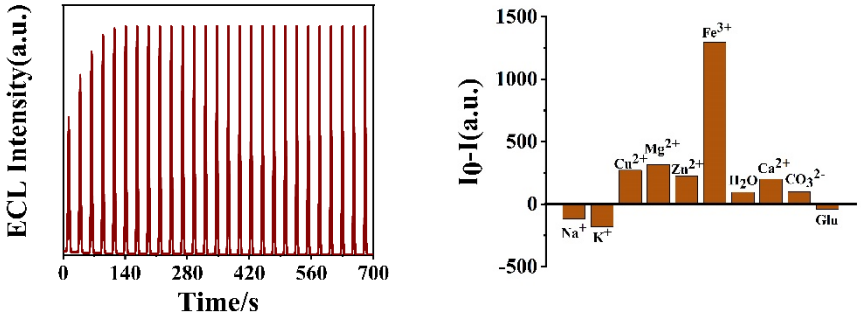

(**a**) (**b**)

Figure 7. (**a**) The stability of P-3/ITO sensor; (**b**) the selectivity of P-3/ITO sensor to Fe^{3+} in the presence of different interfering substances (I_0 and I are the ECL intensity of the sensor before and after adding the different substances, respectively).

The selectivity of the ECL sensor for the analyte is important. In this work, possible interfering substances in river water and serum were selected to explore the selectivity of P-3/ITO for Fe^{3+} detection, including NaCl, KCl, $CuSO_4$, $MgCl_2$, $ZnCl_2$, $CaCl_2$, Na_2CO_3, and glucose with a concentration of 100 μmol/L. The results are shown in Figure 7b that the ECL intensity of P-3/ITO was obviously quenched in the presence of Fe^{3+} (10 μmol/L) compared to other substances, including Na^+, K^+, Cu^{2+}, Ca^{2+}, Mg^{2+}, Zn^{2+}, CO_3^{2+}, and glucose. This indicated that the ECL sensor has good selectivity for Fe^{3+} detection.

With the increase in Fe^{3+} concentration, the ECL signal intensity of P-3/ITO gradually decreased, and the solution gradually became turbid until precipitation appeared. At the same time, the unique irritating odor of TPrA gradually disappeared. When the precipitate was removed, the ECL signal of the supernatant was still weak, indicating that the signal decay process was irreversible. As a result, the ECL decline was attributed to the consumption of the co-reactant TPrA or the luminescent material rather than the darkening of the electrode by the precipitate. Considering the stability of P-3 and the weak alkalinity of the reaction environment, a possible mechanism was proposed regarding the reduction

in the ECL signal of P-3/ITO. Fe^{3+} and P-3 will compete for the co-reactant TPrA, but Fe^{3+} will preferentially transfer electrons to TPrA and form Fe^{2+}, consuming the co-reactant. Next, there may be two pathways for further reducing the ECL signal: (1) Fe^{3+} will form a complex with P-3, which consumes the luminescent material and reduces the ECL signal. (2) In the presence of organic bases such as TPrA, Fe^{3+} may produce the precipitation of Fe $(OH)_3$, which will further consume TPrA.

In order to further explore the experimental mechanism, the precipitates were purified with NMP, ethanol, and H_2O, and analyzed with XRD and IR. It can be seen from Figure 8a that the precipitate has an amorphous structure, indicating that the precipitate is not Fe $(OH)_3$. Furthermore, it can be seen from Figure 8b that the precipitate contains organic groups such as C=O and C-H, and alkyl stretching vibrations of C-H at 2929 cm^{-1} disappeared, which indicated that the second guess may be right, and implied that the precipitate was a complex formed by Fe^{3+} and P-3.

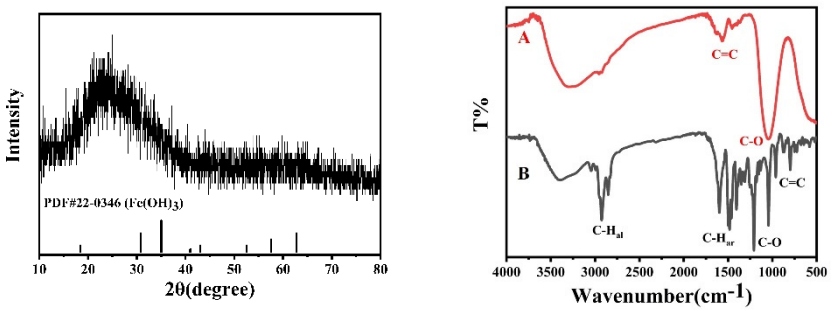

Figure 8. (**a**) XRD of the precipitate; (**b**) IR of precipitate and P-3, the (A) red line is the precipitate and the (B) black line is the P-3.

The generation of and change in ECL on this platform go through two stages (P-3 is represented as P).

Stage 1:

The excited state of P was formed via transferring electrons from TPrA to $P^{+\cdot}$.

$$P - e^- \rightarrow P^{+\cdot} \quad (3)$$

$$TPrA - e^- \rightarrow TPrA^{+\cdot} \quad (4)$$

$$TPrA^{+\cdot} - H \rightarrow TPrA^{\cdot} \quad (5)$$

$$P^{+\cdot} + TPrA^{\cdot} \rightarrow TPrA + P^* \quad (6)$$

$$P^* \rightarrow P + hv \quad (7)$$

Stage 2:

In the presence of Fe^{3+}, TPrA was preferentially consumed by Fe^{3+}, and P can combine with Fe^{3+} to form a complex.

$$TPrA^{\cdot} + Fe^{3+} \rightarrow TPrA + Fe^{2+} \quad (8)$$

After forming a complex, the luminescent material was gradually consumed, therefore the ECL signal of the platform gradually decreased.

The reaction mechanism is shown in Scheme 2.

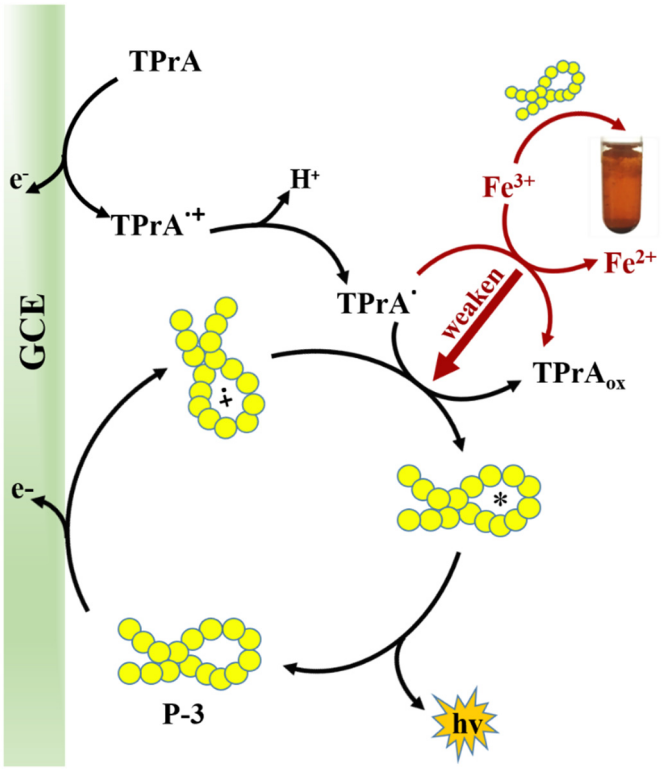

Scheme 2. The possible reaction mechanism: intermolecular electron transfer between P-3 and TPrA and the competition of P-3 and Fe^{3+} for TPrA.

4. Conclusions

In this work, four novel PCMB-Ds with different alkyl side chains have been designed and synthesized. All obtained PCMB-Ds display good solubility and thermal stability, and can emit a strong ECL signal in the presence of TPrA, which provided an ideal alternative polymer ECL reagent. In addition, we explored the relationship between the structure of PCMB-Ds and their ECL performance. Meanwhile, we found that the ECL signal of PCMB-D is enhanced with increasing DP, and the length of the alkyl side chain had little effect. It is proved that the structure of PCMB-D has a certain influence on its ECL performance, which will provide ideas for the preparation of polymer ECL materials in the future. Moreover, based on the preferred P-3, a solid-phase ECL sensor has been constructed, which presents high selectivity to Fe^{3+} and the LOD is 2×10^{-8} mol/L. Furthermore, the mechanism is explored that Fe^{3+} and P-3 competed for the TPrA during the detection process and causes the ECL signal change in P-3/ITO. To our knowledge, this is the first report of polycarbazole materials used in ECL sensors, which will open a new avenue for polycarbazole materials in the field of ECL analysis.

Supplementary Materials: The following supporting information can be downloaded at: https://www.mdpi.com/article/10.3390/polym14153045/s1. Figure S1: ^{1}H NMR spectrum of M1 in $CDCl_3$ at 298 K; Figure S2: ^{1}H NMR spectrum of M2 in DMSO at 298 K; Figure S3: ^{1}H NMR spectrum of M3 in DMSO at 298 K; Figure S4: ^{1}H NMR spectrum of M4 in DMSO at 298 K; Figure S5: ^{1}H NMR spectrum of M5 in DMSO at 298 K; Figure S6: ^{1}H NMR spectrum of P-1 in DMSO at 298 K; Figure S7: ^{13}C NMR spectrum of P-1 in DMSO at 298 K; Figure S8: ^{1}H NMR spectrum of P-2 in $CDCl_3$ at 298 K; Figure S9: ^{13}C NMR spectrum of P-2 in $CDCl_3$ at 298 K; Figure S10: ^{1}H NMR spectrum of P-3 in $CDCl_3$ at 298 K; Figure S11: ^{13}C NMR spectrum of P-3 in $CDCl_3$ at 298 K; Figure S12: ^{1}H NMR spectrum of P-4 in $CDCl_3$ at 298 K; Figure S13: ^{13}C NMR spectrum of P-4 in $CDCl_3$ at 298 K; Figure S14: FTIR spectrum of P-1, al and ar are the abbreviations of alkyl and aromatic ring, respectively; Figure S15: FTIR spectrum of P-2; Figure S16: FTIR spectrum of P-3; Figure S17: FTIR spectrum of P-4; Figure S18: Absorption spectra and emission spectra of P-1, P-2, P-3, and P-4 in

different polarity solvents; Figure S19: Photograph of P-3 in NMP under sunlight and UV light; Figure S20: Aggregation effect of P-3; Figure S21: TGA curves of P-1, P-2, P-3, and P-4 in the presence of nitrogen; Figure S22: Calculated HOMO–LUMO enegy levels for structural models of P-1, P-2, P-3, and P-4.

Author Contributions: Conceptualization, X.Z. and Q.L. (Qian Lu); Data curation, C.Q. and H.Z.; Formal analysis, S.C.; Funding acquisition, X.Z.; Investigation, P.H.; Methodology, X.Z. and S.C.; Project administration, P.H. and Q.L. (Qian Lu); Resources, X.Z.; Software, S.C.; Supervision, X.Z.; Validation and Visualization, P.H. and Q.L. (Qiang Liu); Writing—original draft, P.H.; Writing—review and editing, X.Z. All authors have read and agreed to the published version of the manuscript.

Funding: This research was funded by Universities Twenty Foundational Items of Jinan City (grant number 2021GXRC097), Shandong Provincial Natural Science Foundation (grant number ZR2020MB062), the National Natural Science Foundation of China (grant number NSFC51403111), and Guangdong Provincial Key Laboratory of Applied Botany (grant number AB202105).

Institutional Review Board Statement: Not applicable.

Informed Consent Statement: Not applicable.

Data Availability Statement: The data used to support the findings of this study are available from the corresponding author upon request.

Acknowledgments: We are particularly grateful to the funding support from Qilu University of Technology for talents.

Conflicts of Interest: The authors declare no conflict of interest. The funders had no role in the design of the study; in the collection, analyses, or interpretation of data; in the writing of the manuscript, or in the decision to publish the results.

References

1. Hyder, A.; Buledi, J.A.; Nawaz, M.; Rajpar, D.B.; Shah, Z.-H.; Orooji, Y.; Yola, M.L.; Karimi-Maleh, H.; Lin, H.; Solangi, A.R. Identification of heavy metal ions from aqueous environment through gold, Silver and Copper Nanoparticles: An excellent colorimetric approach. *Environ. Res.* **2022**, *205*, 112475. [CrossRef] [PubMed]
2. Dutt, S.; Hamza, I.; Bartnikas, T.B. Molecular Mechanisms of Iron and Heme Metabolism. *Annu. Rev. Nutr.* **2022**, *42*. *in press*. [CrossRef]
3. Stoyanovsky, D.A.; Tyurina, Y.Y.; Shrivastava, I.; Bahar, I.; Tyurin, V.A.; Protchenko, O.; Jadhav, S.; Bolevich, S.B.; Kozlov, A.V.; Vladimirov, Y.A. Iron catalysis of lipid peroxidation in ferroptosis: Regulated enzymatic or random free radical reaction? *Free Radic. Biol. Med.* **2019**, *133*, 153–161. [CrossRef] [PubMed]
4. Puig, S.; Ramos-Alonso, L.; Romero, A.M.; Martínez-Pastor, M.T. The elemental role of iron in DNA synthesis and repair. *Metallomics* **2017**, *9*, 1483–1500. [CrossRef] [PubMed]
5. Kim, Y.S.; Lee, J.J.; Lee, S.Y.; Jo, T.G.; Kim, C. A highly sensitive benzimidazole-based chemosensor for the colorimetric detection of Fe (II) and Fe (III) and the fluorometric detection of Zn (II) in aqueous media. *RSC Adv.* **2016**, *6*, 61505–61515. [CrossRef]
6. Omeje, K.O.; Ezema, B.O.; Okonkwo, F.; Onyishi, N.C.; Ozioko, J.; Rasaq, W.A.; Sardo, G.; Okpala, C.O.R. Quantification of Heavy Metals and Pesticide Residues in Widely Consumed Nigerian Food Crops Using Atomic Absorption Spectroscopy (AAS) and Gas Chromatography (GC). *Toxins* **2021**, *13*, 870. [CrossRef] [PubMed]
7. Khachatryan, G.; Khachatryan, K. Starch based nanocomposites as sensors for heavy metals-detection of Cu^{2+} and Pb^{2+} ions. *Int. Agrophys.* **2019**, *33*, 121–126. [CrossRef]
8. Ahmad, W.; Bashammakh, A.S.; Al-Sibaai, A.A.; Alwael, H.; El-Shahawi, M.S. Trace determination of Cr(III) and Cr(VI) species in water samples via dispersive liquid-liquid microextraction and microvolume UV-Vis spectrometry. Thermodynamics, speciation study. *J. Mol. Liq.* **2016**, *224*, 1242–1248. [CrossRef]
9. Yan, M.; Gao, W.; Ge, S.; Ge, L.; Chu, C.; Yu, J.; Song, X.; Hou, S. A novel conjugated polyfluorene: Synthesis, characterization and application in label-free ECL immunoassays for biomarker detection. *J. Mater. Chem.* **2012**, *22*, 5568–5573. [CrossRef]
10. Fang, D.; Xu, T.; Fang, L.; Chen, H.; Huang, Y.; Zhang, H.; Miao, Z.; Mao, C.; Chi, B.; Xu, H. A blood compatible, high-efficient sensor for detection of Cr(VI) in whole blood. *Sens. Actuators B Chem.* **2021**, *329*, 129219. [CrossRef]
11. Nemati, F.; Hosseini, M. Recent Advances in Electrochemiluminescence Sensors for Hg^{2+} Ion Detection: A Review. *Anal. Bioanal. Electrochem.* **2021**, *13*, 296–304.
12. Lin, Y.; Gritsenko, D.; Feng, S.; Teh, Y.C.; Lu, X.; Xu, J. Detection of heavy metal by paper-based microfluidics. *Biosens. Bioelectron.* **2016**, *83*, 256–266. [CrossRef] [PubMed]
13. Bertoncello, P. Nanomaterials for biosensing with electrochemiluminescence (ECL) detection. *Front. Biosci.-Landmark* **2011**, *16*, 1084–1108. [CrossRef] [PubMed]

14. Fan, L.; Xiao, G.; Wang, M.; Zhao, S.; Yang, Q.; Cheng, L.; Huang, J.J.; Yue, Z. Ultrasensitive photoelectrochemical microcystin-LR immunosensor using carboxyl-functionalized graphene oxide enhanced gold nanoclusters for signal amplification. *Anal. Chim. Acta* **2021**, *1185*, 339078. [CrossRef]
15. Lee, S.W.; Cho, S.H.; Kang, H.S.; Kim, G.; Kim, J.S.; Jeong, B.; Kim, E.H.; Yu, S.; Hwang, I.; Han, H.; et al. Electroluminescent Pressure-Sensing Displays. *ACS Appl. Mater. Interfaces* **2018**, *10*, 13757–13766. [CrossRef] [PubMed]
16. En-On, J.; Tuantranont, A.; Kerdcharoen, T.; Wongchoosuk, C. Flexible alternating current electroluminescent ammonia gas sensor. *RSC Adv.* **2017**, *7*, 16885–16889. [CrossRef]
17. Wang, N.; Gao, H.; Li, Y.; Li, G.; Chen, W.; Jin, Z.; Lei, J.; Wei, Q.; Ju, H. Dual Intramolecular Electron Transfer for In Situ Coreactant-Embedded Electrochemiluminescence Microimaging of Membrane Protein. *Angew. Chem. Int. Ed.* **2021**, *60*, 197–201. [CrossRef] [PubMed]
18. Xiong, X.; Li, Y.; Yuan, W.; Lu, Y.; Xiong, X.; Li, Y.; Chen, X.; Liu, Y. Screen printed bipolar electrode for sensitive electrochemiluminescence detection of aflatoxin B1 in agricultural products. *Biosens. Bioelectron.* **2020**, *150*, 111873. [CrossRef]
19. Liu, Q.; Fei, A.; Wang, K. An immobilization-free and homogeneous electrochemiluminescence assay for detection of environmental pollutant graphene oxide in water. *J. Electroanal. Chem.* **2021**, *897*, 115583. [CrossRef]
20. Dong, X.; Du, Y.; Zhao, G.; Cao, W.; Fan, D.; Kuang, X.; Wei, Q.; Ju, H. Dual-signal electrochemiluminescence immunosensor for Neuron-specific enolase detection based on "dual-potential" emitter $Ru(bpy)_3^{2+}$ functionalized zinc-based metal-organic frameworks. *Biosens. Bioelectron.* **2021**, *192*, 113505. [CrossRef] [PubMed]
21. Xu, S.; Liu, Y.; Wang, T.; Li, J. Positive potential operation of a cathodic electrogenerated chemiluminescence immunosensor based on luminol and graphene for cancer biomarker detection. *Anal. Chem.* **2011**, *83*, 3817–3823. [CrossRef] [PubMed]
22. Kim, H.J.; Lee, K.-S.; Jeon, Y.-J.; Shin, I.-S.; Hong, J.-I. Electrochemiluminescent chemodosimeter based on iridium(III) complex for point-of-care detection of homocysteine levels. *Biosens. Bioelectron.* **2017**, *91*, 497–503. [CrossRef] [PubMed]
23. Xue, J.; Zhang, Z.; Zheng, F.; Xu, Q.; Xu, J.; Zou, G.; Li, L.; Zhu, J.-J. Efficient Solid-State Electrochemiluminescence from High-Quality Perovskite Quantum Dot Films. *Anal. Chem.* **2017**, *89*, 8212–8216. [CrossRef] [PubMed]
24. Cui, L.; Wang, P.-Y.; Wang, C.-M.; Zhang, C.-Y. Advance in Applications of Organic Polymer. based Electrochemiluminescence in Biochemical Analysis. *Chin. J. Anal. Chem.* **2021**, *49*, 665–675.
25. Goldsmith, S.J. Radioimmunoassay: Review of basic principles. *Semin. Nucl. Med.* **1975**, *5*, 125–152. [CrossRef]
26. Karimi, A.; Husain, S.W.; Hosseini, M.; Azar, P.A.; Ganjali, M.R. Rapid and sensitive detection of hydrogen peroxide in milk by Enzyme-free electrochemiluminescence sensor based on a polypyrrole-cerium oxide nanocomposite. *Sens. Actuators B Chem.* **2018**, *271*, 90–96. [CrossRef]
27. Wang, D.; Wu, C.; Hou, X. Electrochemiluminescence Studies of Phosphorescent Dopant and Host Molecules of Polymer Light-emitting Diodes. *Chin. J. Chem.* **2010**, *28*, 1395–1399. [CrossRef]
28. Li, X.; Li, J.; Wang, H.; Li, R.; Ma, H.; Du, B.; Wei, Q. An electrochemiluminescence sensor for bromate assay based on a new cationic polythiophene derivative. *Anal. Chim. Acta* **2014**, *852*, 69–73. [CrossRef]
29. Grimsdale, A.C.; Chan, K.L.; Martin, R.E.; Jokisz, P.G.; Holmes, A.B. Synthesis of Light-Emitting Conjugated Polymers for Applications in Electroluminescent Devices. *Chem. Rev.* **2009**, *109*, 897–1091. [CrossRef]
30. Li, J.; Xiao, F.-N.; Xia, X.-H. One-step immobilization of $Ru(bpy)_3^{2+}$ in a silica matrix for the construction of a solid-state electrochemiluminescent sensor with high performance. *Analyst* **2012**, *137*, 5245–5250. [CrossRef]
31. Nayana, V.; Kandasubramanian, B. Polycarbazole and its derivatives: Progress, synthesis, and applications. *J. Polym. Res.* **2020**, *27*, 285. [CrossRef]
32. Cimrova, V.; Ulbricht, C.; Dzhabarov, V.; Vyprachticky, D.; Egbe, D.A.M. New electroluminescent carbazole-containing conjugated polymer: Synthesis, photophysics, and electroluminescence. *Polymer* **2014**, *55*, 6220–6226. [CrossRef]
33. Bekkar, F.; Bettahar, F.; Moreno, I.; Meghabar, R.; Hamadouche, M.; Hernaez, E.; Vilas-Vilela, J.L.; Ruiz-Rubio, L. Polycarbazole and Its Derivatives: Synthesis and Applications. A Review of the Last 10 Years. *Polymers* **2020**, *12*, 2227. [CrossRef] [PubMed]
34. Gao, Z.; Zhang, X.; Xing, S.; Lu, Q.; Yao, J.; Liu, Q.; Qiao, C.; Xie, R.; Ding, B. Conjugated polymer nanoparticles based on carbazole for detecting ferric ion (III) with a large Stokes shift and high sensitivity and the application in cell imaging. *Dye. Pigment.* **2019**, *168*, 68–76. [CrossRef]
35. Frisch, M.J.; Trucks, G.W.; Schlegel, H.B.; Scuseria, G.E.; Robb, M.A.; Cheeseman, J.R.; Scalmani, G.; Barone, V.; Petersson, G.A.; Nakatsuji, H. *Gaussian 16 Revision C*; Gaussian Inc.: Wallingford, CT, USA, 2016.
36. Chai, J.-D.; Head-Gordon, M. Long-range corrected hybrid density functionals with damped atom–atom dispersion corrections. *Phys. Chem. Chem. Phys.* **2008**, *10*, 6615–6620. [CrossRef]
37. Frisch, M.J.; Pople, J.A.; Binkley, J.S. Self-consistent molecular orbital methods 25. Supplementary functions for Gaussian basis sets. *J. Chem. Phys.* **1984**, *80*, 3265–3269. [CrossRef]
38. Chen, Y.; Sun, X.; Pan, W.; Yu, G.; Wang, J. Fe^{3+}-sensitive carbon dots for detection of Fe^{3+} in aqueous solution and intracellular imaging of Fe^{3+} inside fungal cells. *Front. Chem.* **2020**, *7*, 911. [CrossRef]
39. Zhao, L.; Wang, Y.; Zhao, X.; Deng, Y.; Xia, Y. Facile synthesis of nitrogen-doped carbon quantum dots with chitosan for fluorescent detection of Fe^{3+}. *Polymers* **2019**, *11*, 1731. [CrossRef]
40. Jayaweera, S.; Yin, K.; Hu, X.; Ng, W.J. Facile preparation of fluorescent carbon dots for label-free detection of Fe^{3+}. *J. Photochem. Photobiol. Chem.* **2019**, *370*, 156–163. [CrossRef]

41. Wang, X.; Li, R.; Fan, S.; Li, Z.; Wang, G.; Gu, Z.; Liu, J. D-penicillamine-functionalized graphene quantum dots for fluorescent detection of Fe^{3+} in iron supplement oral liquids. *Sens. Actuators B Chem.* **2017**, *243*, 211–220. [CrossRef]
42. Liu, Z.; Jia, R.; Chen, F.; Yan, G.; Tian, W.; Zhang, J.; Zhang, J. Electrochemical process of early-stage corrosion detection based on N-doped carbon dots with superior Fe^{3+} responsiveness. *J. Colloid Interface Sci.* **2022**, *606*, 567–576. [CrossRef] [PubMed]